

PROBE3.0: A Systematic Framework for Design-Technology Pathfinding with Improved Design Enablement

Suhyeong Choi, *Graduate Student Member, IEEE*, Jinwook Jung, *Member, IEEE*, Andrew B. Kahng, *Fellow, IEEE*, Minsoo Kim, *Member, IEEE*, Chul-Hong Park, *Member, IEEE*, Bodhisatta Pramanik, *Graduate Student Member, IEEE*, and Dooseok Yoon, *Graduate Student Member, IEEE*

Abstract—We propose a systematic framework to conduct design-technology pathfinding for PPAC in advanced nodes. Our goal is to provide configurable, scalable generation of process design kit (PDK) and standard-cell library, spanning key scaling boosters (backside PDN and buried power rail), to explore PPAC across given technology and design parameters. We build on [6], which addressed only area and cost (AC), to include power and performance (PP) evaluations through automated generation of full design enablements. We also improve the use of artificial designs in the PPAC assessment of technology and design configurations. We generate more realistic artificial designs by applying a machine learning-based parameter tuning flow to [16]. We further employ *clustering-based cell width-regularized placements* at the core of routability assessment, enabling more realistic placement utilization and improved experimental efficiency. We demonstrate PPAC evaluation across scaling boosters and artificial designs in a predictive technology node.

I. INTRODUCTION

Due to the slowdown of dimension scaling relative to the trend of the traditional Moore’s Law, scaling boosters, such as backside power delivery networks (BSPDN), buried power rails (BPR), are introduced at advanced technology nodes. Since scaling boosters play an important role to optimize power, performance, area and cost (PPAC) of advanced technologies, accurate and fast evaluations and predictions of PPAC are critical at an early stage of technology development. Also, use of scaling boosters makes evaluations and predictions of technology more difficult since they introduce a large number of knobs to contribute PPAC improvement.

Design-Technology Co-Optimization (DTCO) is now a well-known key element to develop advanced technology nodes and designs in the modern VLSI chip design. Today’s DTCO spans assessment and co-optimization across almost all components of semiconductor technology and design enablement. As described in Figure 1, the DTCO process consists of three stages: *Technology*, *Design Enablement*, and *Design*. First, the technology stage includes modeling and simulation methodologies for process and device technology. Second, the design enablement stage includes creation of required process design kits (PDK) for the ensuing design stage; these include device models, standard-cell libraries, routing technology files and interconnect parasitic (RC) models. Last, the design stage includes logic synthesis and place-and-route (P&R) based on the generated PDKs from the design enablement stage.

To evaluate and predict technology and design at advanced nodes, all three stages must be correctly performed, and PDKs

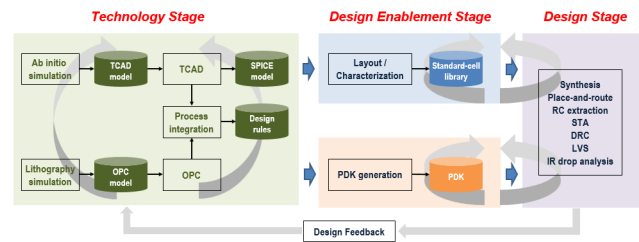


Fig. 1. The DTCO process consists of three main stages: *Technology*, *Design Enablement*, and *Design*. Figure is redrawn from [47].

must be generated from technology and design enablement stages. However, the DTCO process is not simple: feedback from design stage to technology stage takes weeks to months of turnaround time, along with immense engineering efforts. Also, based on the design feedback, additional PDKs may need to be generated at the design enablement stage, which requires additional weeks to months. In order to reduce the turnaround time and maximize the benefit of the DTCO process, a fast and accurate DTCO methodology is needed to assess PPAC with reasonable turnaround time, and to more precisely guide multi-million dollar decisions at an early stage of technology development.

Contributions of Our Work. Compared to the previous works PROBE1.0 [13] and PROBE2.0 [6], our new framework provides three main technical achievements.

(1) **We establish the first comprehensive end-to-end design and technology pathfinding framework.** [6][13] focus on area and cost without considering power and performance. Thus, there is a significant discrepancy between [6][13] and the actual DTCO process in the industry. In this work, we propose a more complete and systematic PROBE3.0 framework, which incorporates power and performance aspects for design-technology pathfinding at an early stage of technology development. PROBE3.0 enables fast and accurate PPAC evaluations by generating configurable PDKs, including standard-cell libraries.

(2) **We improve our designs for PPAC explorations.** Design is a critical factor for PPAC explorations, and artificially generated designs enable us to explore a wider solution space. We leverage [16] to generate artificial designs. To create more realistic artificial designs, we develop a machine learning (ML)-based parameter tuning flow built on [16] to find the best input parameters for generating such designs.

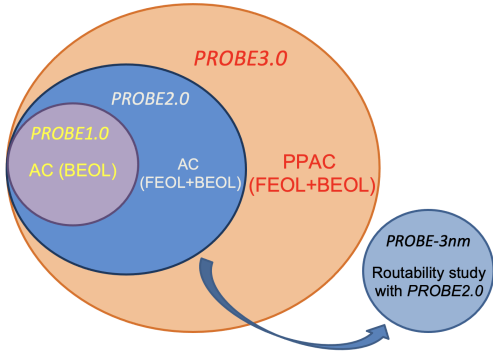


Fig. 2. Scope of PROBE-related works. *PROBE1.0* [13] and *PROBE2.0* [6] address AC given BEOL and FEOL/BEOL, respectively. *PROBE-3nm* [7] studies routability (AC) with sub-3nm technology configurations. *PROBE3.0* provides true full-stack PPAC pathfinding with automatic generation of EDA tool enablements.

Section V details our artificial design generation flow. Further, *cell width-regularization* is employed in [6][13] to prevent illegal placements when swapping neighboring cells to assess the routability metric, K_{th} . We propose a *clustering-based cell width-regularization* to achieve more realistic utilization (and faster routability assessment) as described in Section VI.

(3) **We demonstrate the PPAC exploration of scaling boosters.** We incorporate scaling boosters (BSPDN and BPR) to support P&R and IR drop analysis flows within the framework, as detailed in Section IV. Our results show that incorporating BSPDN and BPR leads to a reduction in power consumption by up to 8% and area by up to 24% based on our predictive 3nm technology. The area reduction results are consistent with those reported in previous industry works [10][22][29][31], which have demonstrated area reductions of 25% to 30% through the use of BSPDN and BPR techniques.

Due to limited access to advanced technology for academic research, we build our predictive 3nm technology, named *the PROBE3.0 technology*. To calibrate the technology, we refer to the International Roadmap for Devices and Structures (IRDS) [40], open-sourced PDKs, and other publications [2][8][23][37]. We open-source our work, including process design kits (PDKs), standard-cell libraries, and scripts for P&R and IR drop analysis; this is available in our GitHub repository [48]. In Section III, we provide details on the automated PDKs and library generation flows, while in Section VII, we present three experiments to demonstrate the effectiveness of the *PROBE3.0* framework for PPAC pathfinding.

II. RELATED WORK

In this section, we divide the relevant previous works into the three categories of (i) advanced-technology research PDKs, (ii) design-technology co-optimization and (iii) scaling boosters, along with (iv) “PROBE” frameworks.

Advanced Technology Research PDKs. PDKs of advanced node technologies are highly confidential. Academic research can be blocked by limited access to relevant information. To unblock academic research, predictive advanced-node PDKs have been published. ASAP7 [8] is a predictive PDK for 7nm FinFET technology that includes standard cells which support commercial logic synthesis and P&R. FreePDK3 [23][37] and

FreePDK15 [2] are open-source PDKs for 3nm and 15nm technology. [15] proposes a 3nm predictive technology called NS3K with nanosheet FETs (NSFET). The authors of [15] also create 5nm FinFET and 3nm NSFET libraries to compare power, performance and area.

Design-Technology Co-Optimization. Previous DTCO works evaluate block-level PPAC and optimize design and technology simultaneously. [25] proposes UTOPIA to evaluate block-level PPAC with thermally limited performance, and to optimize device and technology parameters. [18] proposes a fast pathfinding DTCO flow for FinFET and complementary FET (CFET). [3] also proposes a fast and agile technology pathfinding platform with compact device models to accelerate the DTCO process. [12] describes power delivery network pathfinding for 3D IC technology to study tradeoffs between IR drop and routability. [5] uses ML to predict sensitivities to changes for DTCO.

Scaling Boosters. As described in Section I, scaling boosters are used in advanced nodes to maximize benefit of new technology. BSPDN and BPR are among the most promising scaling boosters in sub-5nm nodes. [21] carries out a CPU implementation with BSPDN and BPR in their 3nm technology, demonstrating a reduction of up to 7X in worst IR drop. Similarly, [22] investigates BSPDN and BPR at sub-3nm nodes and finds that they can lead to a 30% reduction in area based on IR drop mitigation. [4] also explores the impact of BSPDN and BPR on design, concluding that their use can lead to a 43% reduction in area with 4X less IR drop. [10] studies BSPDN configurations with μ TSVs, and observes 25% to 30% reduction in area using BSPDN and BPR. Additionally, [24] investigates BSPDN with nTSVs and μ TSVs and finds that the average IR drop with BSPDN improves by 69% compared to traditional frontside PDN (FSPDN). Finally, [27] conducts holistic evaluations for BSPDN and BPR, demonstrating that FSPDN with BPR achieves a 25% lower on-chip IR drop, while BSPDN with BPR achieves an 85% lower on-chip IR drop with iso-performance and iso-area. In contrast to these previous DTCO works, here we propose a highly *configurable* framework that enables more efficient investigation of scaling boosters in advanced nodes.

“PROBE” Frameworks. Prior “PROBE” [6][13] works propose systematic frameworks for assessing routability with different FEOL and BEOL configurations. Specifically, [13] begins with an easily-routable placement and increases the routing difficulty by random neighbor-swaps until the routing fails with greater than a threshold number of design rule violations (DRCs). The normalized number of swaps at which routing failure occurs, denoted by K_{th} , is a metric used to measure the inherent routability of the given parameters. On the other hand, [6] introduces an automatic standard-cell layout generation using satisfiability modulo theory (SMT) to support explorations of both FEOL and BEOL configurations. The authors of [6] also employ machine learning (ML)-based K_{th} prediction to expedite the DTCO pathfinding process. Additionally, [7] employs *PROBE2.0* in a routability study with sub-3nm technology configurations.

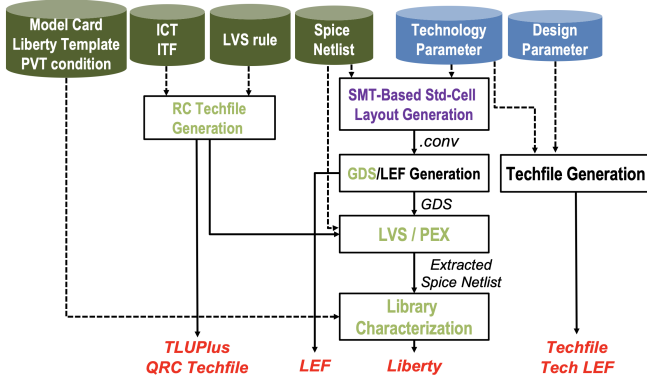


Fig. 3. Automatic standard-cell library and PDK generation (*Design Enablements*) in the PROBE3.0 framework. In addition to technology and design parameters in the PROBE3.0 framework, other technology-related inputs are required: (i) Device model cards, (ii) Liberty templates, (iii) Process/Voltage/Temperature (PVT) conditions, (iv) Interconnect technology files (ICT or ITF formats), (v) LVS rules, and (vi) SPICE netlists.

III. STANDARD-CELL LIBRARY AND PDK GENERATION

Expediting the DTCO process requires automation of the standard-cell library and PDK generation flows. Therefore, the PROBE2.0 framework [6] introduces standard-cell layout and PDK generation flows and utilizes them for routability assessments. In this work, we extend the PROBE2.0 framework to include proper electrical models of standard-cell libraries and interconnect layers for design-technology pathfinding. Additionally, we enhance the PDK generation flow to support advanced nodes. While the PROBE2.0 framework solely focuses on the physical layout of standard cells, the PROBE3.0 framework enables true full-stack PPAC pathfinding through automated, configurable standard-cell and PDK generation flows for advanced nodes. To demonstrate use of PROBE3.0 for advanced-node PPAC pathfinding, we use a technology that incorporates cutting-edge (3nm FinFET) technology predictions based on the works of [8][40].

A. Overall flow

Figure 3 describes our overall flow of standard-cell and PDK generation. Technology and design parameters are defined as input parameters for the flow. Beyond these input parameters, there are additional inputs required to generate standard-cell libraries and PDKs, as follows: (i) SPICE model cards, (ii) Liberty template and PVT conditions, (iii) Interconnect technology files (ICT/ITF), (iv) LVS rule deck, and (v) SPICE netlists. Given the inputs, our SMT-based standard-cell layout generation and GDS/LEF generation are executed sequentially. Generation of timing and power models (Liberty) requires additional steps including LVS, parasitic extraction and library characterization flow. Aside from the standard-cell library generation, we also generate interconnect models from ICT/ITF, and P&R routing technology files from technology and design parameters. The PDK elements that we generate feed seamlessly into commercial logic synthesis and P&R tools. Further, to the best of our knowledge, ours is the first-ever work that is able to disseminate all associated EDA tool scripts for research purposes.

B. PROBE3.0 Technology

We build our own predictive 3nm technology node, called *the PROBE3.0 technology*. Based on [8], we define our FEOL

TABLE I
LAYER DEFINITION IN THE PROBE3.0 TECHNOLOGY.

Layer	Name	Description
FEOL	WELL	N-Well
	FIN	Fin
	GATE	Poly (gate)
	GCUT	Gate cut
	ACTIVE	Active area for fin definition
	NSELECT	N-implant
	PSELECT	P-implant
	CA	Contact (via) between LIG/LISD and M0
	LIG	Gate interconnect layer
	LISD	Source-drain interconnect layer
	SDT	Source-drain trench (ACTIVE to LIG/LISD)
	BOUNDARY	Boundary layer for P&R
BEOL	M0-M13	Metal layers
	V0-V12	Via layers

TABLE II
KEY FEATURES OF THE PROBE3.0 TECHNOLOGY.

Layer	Feature	Value
FEOL	Fin Pitch	24 nm
	Fin Width	6 nm
	Gate Pitch (CPP)	45 nm
	Gate Width	16 nm
	Standard-Cell Height	100 / 120 / 144 nm
	Dielectric constant	3.9
BEOL	Aspect Ratio (width/thickness)	1.5
	Power/Ground Pin Width (M0)	36 nm
	M0/M2/M3 pitch	24 nm
	M1 pitch	30 nm
	M4-M11 pitch	64 nm
	M12-M13 / BM1-BM2 pitch	720 nm
	V0-V3 via resistance	50 ohm/via
	V4-V11 via resistance	5 ohm/via
	V12 via resistance	0.06294 ohm/via
Dielectric constant	2.5-3	

and BEOL layers as described in Table I. We assume that all BEOL layers are unidirectional routing layers. Hence, we first change M1 to a unidirectional routing layer with vertical preferred direction, since the work of [8] has a bidirectional M1 routing layer. We add an M0 layer with horizontal preferred direction below the modified M1 layer, and we add contact layers V0 and CA which respectively connect between M1 and M0, and between gate/source-drain and M0.

Also, electrical features of technologies are critical to explore “PP” aspects. Therefore, parasitic extractions of standard cells and BEOL metal stacks are important steps. To extract parasitic elements, interconnect technology files are required to use commercial RC extraction, P&R and IR drop analysis tools. In this work, we use commercial tools [35][43][46] for extractions, and each tool has its own technology file format.¹ Interconnect technology files include layer structures of technology and electrical parameters, such as thickness, width, resistivity, dielectric constant and via resistance. We refer to the values of physical features in the 3nm FinFET technology of [40], such as fin pitch, fin width, gate pitch, gate width, metal pitch and aspect ratio. We also refer to [40] for the values for electrical parameters such as via resistance and dielectric constant. Table II describes key features of the PROBE3.0 technology.

¹The file formats for each tool are unique. The MIPT file format is for *Siemens Calibre* [43] for extraction, and is converted to an RC rule file for standard-cell layout extractions. On the other hand, the ICT and ITF file formats are for *Cadence* and *Synopsys* extraction tools, respectively. We convert ICT to QRC techfile, and ITF to TLUPlus file, to enable P&R tools and IR drop analysis.

TABLE III
LIST OF 41 STANDARD CELLS PER GENERATED LIBRARY.

Cell List	Size
Inverter (INV), Buffer (BUF)	X1, X2, X4, X8
2-input AND/OR/NAND/NOR (AND2/OR2/NAND2/NOR2)	X1, X2
3-input AND/OR/NAND/NOR (AND3/OR3/NAND3/NOR3)	X1, X2
4-input NAND/NOR (NAND4/NOR4)	X1, X2 </td
2-1 AND-OR-Inverter (AOI21), 2-2 AND-OR-Inverter (AOI22)	X1, X2
2-1 OR-AND-Inverter (OAI21), 2-2 OR-AND-Inverter (OAI22)	X1, X2
D flip-flop (DFFHQ), D flip-flop with reset (DFFRNQ)	X1
2-input MUX/XOR (MUX2/XOR2), Latch (LHQ)	X1

C. Improved Standard-Cell Library Generation

We generate standard-cell libraries via several steps illustrated in Figure 3: (i) SMT-based standard-cell layout generation, (ii) generation of GDS and LEF files, (iii) LVS and PEX flow, and (iv) library characterization flow.

SMT-Based Standard-Cell Layout Generation. In recent technology nodes, standard-cell architectures use a variety of pitch values for different layers in order to optimize power, performance, area and cost (PPAC). To accommodate this, PROBE3.0 improves the SMT-based layout generation used in PROBE2.0 to support non-unit gear ratios for M1 pitch (M1P) and contacted poly pitch (CPP).

Our standard-cell layouts are generated using SPICE netlists, technology and design parameters from [6]. However, in PROBE3.0 we change two key parameters: metal pitch (MP) and power delivery network (PDN). Instead of using MP, we define parameters for pitch values of each layer. Since M0, M1 and M2 layers are used for standard-cell layouts, we define M0P, M1P and M2P as pitches of M0, M1 and M2 layers, respectively. Table 4 shows four layouts of AND2_X1 cells with four parameter settings. The four standard-cell libraries (*Lib1*, *Lib2*, *Lib3* and *Lib4*) along with their corresponding parameter sets are used for our experiments in Section VII. For our PPAC exploration, we generate 41 standard cells for each standard-cell library as shown in Table III.

GDS/LEF Generation and LVS/PEX Flow. While [6] only supports LEF generation for P&R, PROBE3.0 generates standard-cell layouts in both GDS and LEF formats. The GDS files are used to extract parasitics from standard-cell layouts and check LVS between layouts and schematics. We use *Calibre* [43] to check LVS and generate extracted netlists for standard cells with intra-cell RC parasitics. Scripts for GDS/LEF generation and LVS/PEX flows are open-sourced in [48].

Library Characterization Flow. We perform library characterization to generate standard-cell libraries in the Liberty format. The inputs to the flow are model cards for FinFET devices, Liberty template including PVT conditions, and interconnect technology files. We use model cards from [37]. For the Liberty template, we define the PVT conditions, and the capacitance and transition time indices of (7×7) tables for electrical models (delay, output transition time, and power). We use 5, 10, 20, 40, 80, 160, and 320ps as the transition time indices. For the input capacitance, we obtain the input pin capacitance C_{inv} of an X1 inverter, then multiply this value by predefined multipliers, 2, 4, 8, 16, 24, 32, and 64. For characterization, we use the PVT corner ($TT, 0.7V, 25^\circ C$).

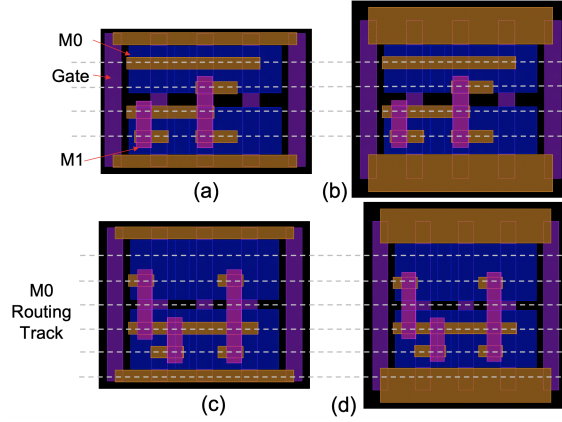


Fig. 4. Example standard cells (AND2_X1) in this work. The cells are generated by our SMT-based standard-cell layout generation with the following parameters (Fin , RT , $PGpin$, CH): (a) *Lib1* ($2Fin$, $4RT$, BPR , $5T$); (b) *Lib2* ($2Fin$, $4RT$, $M0$, $6T$); (c) *Lib3* ($3Fin$, $5RT$, BPR , $6T$); and (d) *Lib4* ($3Fin$, $5RT$, $M0$, $7T$).

IV. POWER DELIVERY NETWORK

We study PDN scaling boosters to showcase the DTCO and pathfinding capability of PROBE3.0. There are two key challenges of traditional PDNs at advanced technologies:

- *High resistance of BEOL* [19]: Elevated resistance in BEOL layers exacerbates IR drop issues, necessitating denser PDN topologies.
- *Routing overheads (routability)* [26]: PDN occupies routing resources that are shared with signal and clock distribution. The routability and area density impact of PDN becomes more severe with denser PDN at advanced nodes.

To overcome these challenges, multiple foundries have begun implementing backside power delivery networks (BSPDN) and buried power rails (BPR) as scaling boosters in their sub-5nm technologies. We use these scaling boosters, BSPDN and BPR, to demonstrate use of PROBE3.0. We establish four options for PDN parameter in the PROBE3.0 framework: (i) Frontside PDN without BPR (P_{FS}); (ii) Frontside PDN with BPR (P_{FB}); (iii) Backside PDN without BPR (P_{BS}); and (iv) Backside PDN with BPR (P_{BB}). Figure 5 illustrates the four PDN configurations in the PROBE3.0 framework.

A. Frontside and Backside Power Delivery Network

We have defined realistic structures for both frontside power delivery networks (FSPDN) and backside power delivery networks (BSPDN), and enabled IR drop analysis within our framework. Table IV shows the configurations for FSPDN and BSPDN. Since BEOL layers with smaller pitches (e.g., 24nm-pitch layer) have high resistance, we add power stripes for every layer. While the work of [6] has multiple options for FSPDN, the PROBE3.0 framework has only one PDN structure for FSPDN. Instead, we add other options such as P_{FB} , P_{BS} and P_{BB} . Furthermore, while the *Backside* option in [6] assumes no PDN at the frontside for the BSPDN option, we add power stripes at the backside for BSPDN in the PROBE3.0 framework to enable IR drop analysis for BSPDN.

Figures 5(a) and (c) respectively show cross-section views of P_{FS} and P_{BS} options. The P_{FS} option has M0 power and ground pins for standard cells, which connect to power stripes

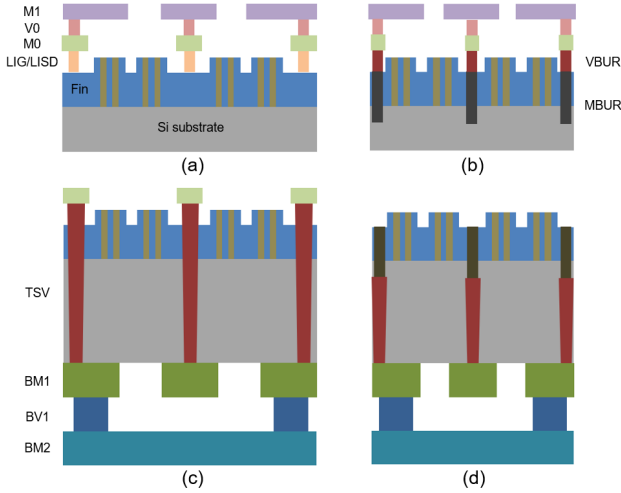


Fig. 5. Cross-section view of four PDN options in the PROBE3.0 framework: (a) Frontside PDN (P_{FS}); (b) Frontside PDN with BPR (P_{FB}); (c) Backside PDN (P_{BS}); and (d) Backside PDN with BPR (P_{BB}).

TABLE IV

PDN CONFIGURATIONS FOR FSPDN AND BSPDN. A PAIR OF POWER (VDD) AND GROUND (VSS) STRIPES ARE PLACED EVERY PITCH, WHILE MAINTAINING THE SPACING BETWEEN VDD AND VSS. *Density* DENOTES THE PERCENTAGE OF ROUTING TRACKS OCCUPIED BY PDN.

PDN	Layer	Pitch (um)	Width (um)	Spacing (um)	Density (%)
FSPDN	M3	1.08	0.012	0.508	4
	M4	1.152	0.032	0.544	11
	M5-M11	5.0	1.0	1.5	20
	M12-M13	4.32	1.8	0.36	100
BSPDN	BM1-BM2	4.32	1.8	0.36	100

at the frontside of the die. The P_{BS} option uses the same M0 power and ground pins for standard cells but connects to power stripes at the backside of the die. For the P_{BS} option, we employ two backside metal layers (BM1 and BM2) and one via layer (BV1) between the backside metal layers. The layer characteristics (width, pitch and spacing) are identical to the top two layers (M12 and M13) of FSPDN. Additionally, the M0 pins of standard cells and BSPDN are connected using Through-Silicon Vias (TSVs). We assume nano-TSVs with 90nm [24] width for the P_{BS} option, and 1:10 width-to-height aspect ratio. For the P_{BS} option, TSV insertions necessitate reserved spaces in front-end-of-line (FEOL) layers, including keepout margins surrounding the TSVs. To accommodate this, we insert *power tap cells* prior to standard-cell placement.

B. Frontside and Backside PDN with Buried Power Rail

In advanced nodes, power rails on BEOL metal layers can be “buried” into FEOL levels with shallow-trench isolation (STI). Using deep trench and creating space between devices lowers the resistance of power rails. In addition to the resistance benefits, standard-cell height (area) can be further reduced with deep and narrow widths of power and ground pins. Figures 5(b) and (d) respectively show cross-section views of FSPDN with BPR (P_{FB}) and BSPDN with BPR (P_{BB}) options. In the case of P_{FB} , connections between FSPDN and BPR are made through nano-TSVs with the same 90nm width as in the P_{BS} option (but, with 1:7 aspect ratio). These nano-TSVs also necessitate insertion of reserved spaces.

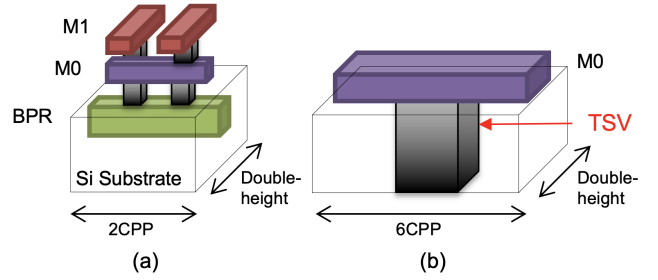


Fig. 6. Power tap cells for (a) P_{FB} and (b) P_{BS} .

C. Power Tap Cell Insertion

Although use of BSPDN and BPR can reduce area and mitigate IR drop problems, connecting frontside layers to BSPDN and/or BPR remains a critical challenge. To establish “tap” connections from frontside metals to BPR, or from backside to frontside metals, space must be reserved on device layers – e.g., [21] proposes power tap cells for the connection between BPR to MINT (M0) layers. More frequent “taps” will mitigate IR drop problems, but occupy more placement area. In PROBE3.0, we define two types of power tap cells for the P_{FB} and P_{BS} options. Tap cells for P_{FB} connect BPR to M1, and tap cells for P_{BS} connect BM1 to M0. By contrast, P_{FS} and P_{BB} do not require power tap cells.

Power Tap Cell Structure. Figure 6(a) shows a structure of power tap cells for P_{FB} . Double-height power tap cells for P_{FB} have 2CPP cell width. The connection between BPR and M0 is through a 1×2 via array, and the two M1 metals are aligned with M1 vertical routing tracks. There are also two types of power tap cells for P_{FB} according to starting power and ground pins: power/ground pins on the double-height power tap cells are ordered as Power-Ground-Power (VDD-VSS-VDD) or Ground-Power-Ground (VSS-VDD-VSS). On the other hand, Figure 6(b) shows a structure of power tap cells for P_{BS} . While power tap cells for P_{FB} have 2CPP width, double-height power tap cells for P_{BS} have 6CPP width due to the ~ 90 nm width of nano-TSVs [24]. We also assume a 50nm keepout spacing around nano-TSVs. Similar to power tap cells for P_{FB} , there are two types of double-height power tap cells for P_{FB} , Power-Ground-Power and Ground-Power-Ground.

Power Tap Cell Insertion Scheme. Power tap cell insertion affects routability and IR drop, and hence affect PPAC of designs. In this work, we define five tap cell insertion pitches and two power tap insertion schemes, as follows.

- I_{pitch} : 24, 32, 48, 96 and 128CPP
- I_{scheme} : *Column* and *Staggered*

I_{pitch} and I_{scheme} denote tap cell insertion pitch and tap cell insertion scheme, respectively. Tap cell insertion scheme *Column* places double-height power tap cells on every two placement rows with the given tap cell pitch. Conversely, tap cell insertion scheme *Staggered* places double-height power tap cells on every four placement rows with the given tap cell pitch. Figure 7 shows four power tap cell insertion results for P_{FB} and P_{BS} with *Column* and *Staggered* insertion schemes.

D. IR Drop Analysis Flow

We develop two IR drop analysis flows for FSPDN and BSPDN. Figure 8(a) presents our IR drop analysis flow for FSPDN. After P&R, we generate DEF and SPEF files for

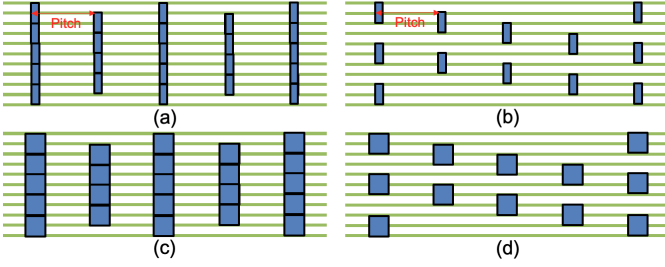


Fig. 7. Four power tap cell insertion results. (a) Power tap cells for P_{FB} (2CPP width) with *Column*; (b) power tap cells for P_{FB} with *Staggered*; (c) power tap cells for P_{BS} (6CPP width) with *Column*; and (d) power tap cells for P_{BS} with *Staggered*.

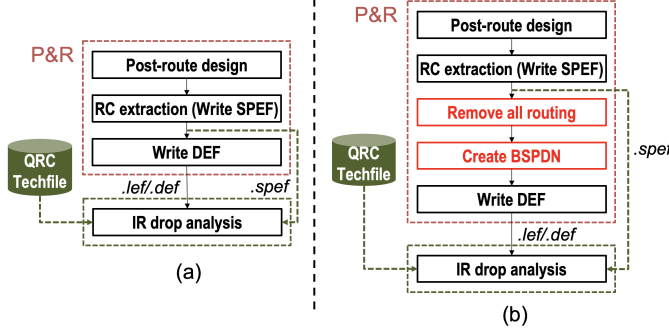


Fig. 8. IR drop analysis flow for (a) FSPDN and (b) BSPDN. For the IR drop flow for BSPDN, we delete all the signal and clock routing after P&R and build power stripes for BSPDN.

routed designs using a commercial P&R tool to perform standalone vectorless dynamic IR drop analysis. Additionally, an interconnect technology file (QRC techfile) is needed for RC extraction as input for the IR drop analysis flow. In contrast, Figure 8(b) depicts our IR drop analysis flow for BSPDN. After P&R, we only create a SPEF file from routed designs. We then remove all routed signals and clocks from the P&R database and construct new power stripes for BSPDN. Since the standalone IR drop analysis tool obtains power stripe information from a DEF file, we generate a DEF file after creating power stripes on the backside. There are two backside metal layers, BM1 and BM2. When creating PDN on backside metal layers, we consider M1 as BM1 and M2 as BM2, respectively. For RC extraction with BSPDN, the QRC techfile must be scaled for backside metals since we assume BM1 and BM2 have the same pitches as M12 and M13. Full details are visible in open-source scripts at [48].

V. ENHANCED ARTIFICIAL DESIGNS FOR PPAC EXPLORATION

The use of specific real designs in DTCO and PPAC exploration can bring risk of biases and incorrect decisions regarding technology configurations (e.g., cell architecture or BEOL stack). To avoid such biases, the PROBE1.0 [13] bases its routability assessment on a mesh-like netlist topology, and PROBE2.0 [6] similarly uses a knight’s tour-based topology. However, these artificial topologies have two main limitations as we bring “PP” aspects of PPAC into the picture. First, they are highly regular and cannot capture a wide range of circuit types. Second, they do not mimic timing and power properties of real netlists, as they target routability assessment without regard to timing path structure.

TABLE V
DEFINITION OF TOPOLOGICAL PARAMETERS IN ANG [16][30].

Parameter	Definition
$N_{inst}(T_1)$	Number of instances.
$N_{prim}(T_2)$	Number of primary inputs/outputs.
$D_{avg}(T_3)$	Average net degree. The net degree of a net is the number of terminals of the net.
$B_{avg}(T_4)$	Average size of net bounding box. The placed (or routed) layout is divided into a bin grid where each bin contains $\sqrt{N_{inst}}$ instances.
$T_{avg}(T_5)$	Average depth of timing paths. The depth of a given timing endpoint is the maximum number of stages in any fanin combinational path of that endpoint. T_{avg} is the average of all endpoint depths.
$S_{ratio}(T_6)$	Ratio of the number of sequential cells to the total number of cells. S_{ratio} equals to number of sequential cells over total number of instances.

PROBE3.0 overcomes these limitations by generating artificial but realistic netlists with the *Artificial Netlist Generator* (ANG) of [16][30], for use in PPAC studies. We use the six topological parameters of ANG (see Table V) to generate and explore circuits with various sizes, interconnect complexity, routed wirelengths and timing. Moreover, we apply machine learning (AutoML) to improve the match of generated artificial netlists to targeted (real) netlists.

A. Comparison of ANG and Real Designs

In this subsection, we study four real designs from OpenCores [41] and the corresponding artificial netlists generated by ANG [16]. Each design is taken through commercial logic synthesis and P&R tools [44][45] in the PROBE3.0 technology, to obtain a final-routed layout. For AES, JPEG, LDPC and VGA, we respectively use target clock periods of 0.2ns, 0.2ns, 0.6ns and 0.2ns, and utilizations of 0.7, 0.7, 0.2 and 0.7. We then extract the six topological parameters from the routed designs and use these parameters to generate artificial netlists with ANG.

We introduce a *Score* metric to quantify similarity between artificial and real netlists, as defined in Equation (1).

$$Score = \prod_{i=1}^N \max\left(\frac{T_i^{target}}{T_i^{out}}, \frac{T_i^{out}}{T_i^{target}}\right) \quad (1)$$

where: T_i^{target} = T_i in target parameter set
 T_i^{out} = T_i of output parameter set
 N = number of parameters ($N = 6$)

In Equation (1), target and output parameters are elements T_i^{target} and T_i^{out} of the target and output parameter sets. For each parameter, we calculate the discrepancy (ratio) between target and output values. The *Score* value is the product of these ratios. Ideally, if output parameters are exactly the same as target parameters, *Score* is 1. Larger values of *Score* indicate greater discrepancy between ANG-generated netlists and the target netlists.

Table VI shows the input parameters, extracted parameters and *Score* metric in our comparison of real and artificial designs. The causes of discrepancy are complex, e.g., [16] has steps that heuristically adjust average depths of timing paths T_{avg} and the ratio of sequential cells S_{ratio} . Also, performing P&R will change the number of instances N_{inst} , the average net degree D_{avg} , and the routing which determines B_{avg} . Hence, it is difficult to identify the input parameterization of ANG that will yield artificial netlists whose post-route

TABLE VI

TOPOLOGICAL PARAMETERS FOR REAL NETLISTS FROM OPENCORES [41] AND ARTIFICIAL NETLISTS GENERATED BY [16]. DESIGN NAMES FOLLOWED BY * INDICATE ANG-GENERATED ARTIFICIAL NETLISTS.

Design	Parameters						Score
	N_{inst}	N_{prim}	D_{avg}	B_{avg}	T_{avg}	S_{ratio}	
AES	12318	394	3.28	0.55	7.98	0.04	-
JPEG	70031	47	3.09	0.21	10.36	0.07	-
LDPC	77379	4102	2.85	1.00	12.94	0.03	-
VGA	60921	185	3.71	0.42	8.25	0.28	-
AES*	10371	394	3.28	0.79	5.19	0.13	8.53
JPEG*	63185	47	3.16	0.70	6.97	0.15	12.03
LDPC*	58699	4106	3.10	0.78	6.96	0.13	14.8
VGA*	64412	188	3.32	0.26	6.39	0.25	2.8

properties match those of (target) real netlists. We use machine learning to address this challenge.

B. Machine Learning-Based ANG Parameter Tuning

We improve the realism of generated artificial netlists with ML-based parameter tuning for ANG. Figure 9(a) shows the training flow in the parameter tuning. First, to generate training data, we sweep the six ANG input parameters to generate 21,600 combinations of input parameters, as described in Table VII. Second, we use ANG with these input parameter combinations to generate artificial gate-level netlists. Third, we perform P&R with the (21,600) artificial netlists and extract the output parameters. The extracted output parameters are used as output labels for the ML model training. We use the open-source H2O AutoML package [39] (version 3.30.0.6) to predict the output parameters; the *StackedEnsemble_AllModels* model consistently returns the best model. The model training is a one-time overhead which took 4 hours using an Intel Xeon Gold 6148 2.40GHz server. Executing commercial P&R required just over 7 days in our academic lab setting, and is again a one-time overhead.²

Figure 9(b) shows our inference flow. First, we define ranges around the target parameter and sweep the parameters to generate multiple combinations of input parameters as candidates, which are shown in Table VII. Second, we use our trained model to predict the output parameters from each input parameter combination. Note that although there are 12.3M combinations as specified in the rightmost two columns of Table VII, this step requires less than 10 minutes on an Intel Xeon Gold 6148 2.40GHz server.³ Third, we calculate a predicted *Score* per each input parameter combination, and then choose the parameter combination with lowest predicted *Score*. Finally, we use ANG and the chosen parameter combination to generate an artificial netlist for P&R and PPAC explorations.

²The average P&R runtime on our 21,600 ANG netlists is 0.4 hours on an Intel Xeon Gold 6148 2.40GHz server. The data generation used 50 concurrently-running licenses of the P&R tool, with each job running single-threaded. $(21,600 \times 0.4 / 50 / 24 \approx 7.2$ days. With multi-threaded runs, we estimate that data generation would have taken 3 to 4 days.)

³ $11 \times 11 \times 21 \times 21 \times 11 \times 21 = 12,326,391$. We apply simple filtering based on lower and upper bounds, to avoid parameter values for which ANG does not work properly. Specifically, parameter values are restricted to be within: $0 < B_{avg} \leq 1.0$; $0 < S_{ratio} \leq 1.0$; $1 < D_{avg} < 2.6$; and $3 < T_{avg}$. For example, the AES testcase then has ~ 3 M input parameter combinations, and predicting output parameters for all of these takes 441 seconds of runtime.

TABLE VII

PARAMETER SETS FOR TRAINING AND TESTING. WE TRAIN OUR ML MODEL WITH ANG INPUT PARAMETERS AND POST-P&R OUTPUT PARAMETERS. THE TOTAL NUMBER OF DATAPOINTS IS $4 \times 6 \times 6 \times 5 \times 5 \times 6 = 21600$. TESTING IS PERFORMED IN THE RANGES AROUND GIVEN TARGET PARAMETERS, ACCORDING TO THE STEP SIZES.

Parameter	Training Value	Testing Value	
		Range	Step
$N_{inst} (T_1^{in})$	10000, 20000, 40000, 80000	$T_1^{target} \pm 500$	100
$N_{prim} (T_2^{in})$	100, 200, 500, 1000, 2000, 4000	$T_2^{target} \pm 5$	1
$D_{avg} (T_3^{in})$	1.8, 2.0, 2.2, 2.4, 2.6	$T_3^{target} \pm 0.2$	0.02
$B_{avg} (T_4^{in})$	0.70, 0.75, 0.80, 0.85, 0.90, 0.95	$T_4^{target} \pm 0.2$	0.02
$T_{avg} (T_5^{in})$	6, 8, 10, 12, 14, 16	$T_5^{target} \pm 10$	2
$S_{ratio} (T_6^{in})$	0.2, 0.4, 0.6, 0.8, 1.0	$T_6^{target} \pm 0.2$	0.02

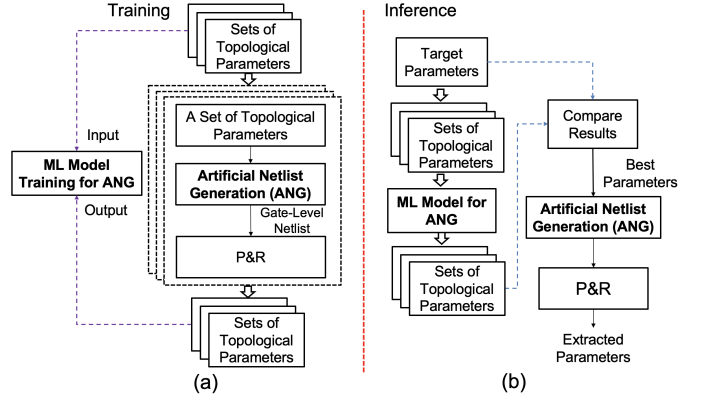


Fig. 9. ML-based parameter tuning for ANG.

Table VIII shows the benefit from ML-based ANG parameter tuning. Columns 2-5 show parameters from real netlists, which we use as target parameters. The trained ML model and the inference flow produce the tuned parameters for ANG shown in Columns 6-9 of the table, and corresponding results are shown in Columns 10-13. The average *Score* decreases from to 4.89 from the original value of 8.87 for ANG without ML-based parameter tuning (Table VI).

The ML-enabled improvement of realism in ANG netlists can be seen using t-SNE visualization [20] from P&R results. We perform P&R for the four real designs by sweeping initial utilization from 0.6 to 0.8 with a 0.01 step size, and target clock period from 0.15 to 0.25ns with a 0.01ns step size; this results in $21 \times 11 = 231$ P&R runs. (For LDPC, we sweep utilization from 0.1 to 0.3 with a 0.01 step size, and clock period from 0.55 to 0.65ns with a 0.01ns step size.) We then perform P&R for artificial netlists with and without our parameter tuning flow, with 0.7 utilization (0.2 for LDPC) and 0.2ns (0.6ns LDPC) target clock period. Figure 10 shows t-SNE visualization⁴ of the real and artificial designs. The 231 real datapoints per design form well-defined clusters. In Figure 10(a), the datapoints of the artificial AES and JPEG designs are located in the corresponding designs' clusters. However, the artificial LDPC and VGA designs are not close to the corresponding clusters of real designs. By contrast,

⁴For t-SNE visualization, we collect ten features from P&R results: Number of instances, number of nets, number of primary input/output pins, average fanout, number of sequential cells, wirelength, area, number of design rule violations, worst negative slack, total negative slack, and number of failing endpoints.

TABLE VIII
 TOPOLOGICAL PARAMETERS FOR TARGET, INPUT AND OUTPUT NETLISTS. THE DESIGN NAMES FOLLOWED BY ** INDICATE ANG-GENERATED ARTIFICIAL NETLISTS WITH ML-BASED ANG PARAMETER TUNING.

Parameter	Parameters of Target Netlists				ANG Input Parameters (ML Inference)				Parameters from Artificial Netlists			
	AES	JPEG	LDPC	VGA	AES	JPEG	LDPC	VGA	AES**	JPEG**	LDPC**	VGA**
N_{inst}	12318	70031	77379	60921	12718	69531	76979	60421	10200	64296	64796	65113
N_{prim}	394	47	4102	185	390	42	4106	199	394	46	4110	202
D_{avg}	3.28	3.09	2.85	3.71	3.40	3.10	3.03	3.53	3.26	3.13	3.18	3.30
B_{avg}	0.55	0.21	1.00	0.42	0.49	0.31	1.98	0.28	0.72	0.21	0.73	0.36
T_{avg}	7.98	10.36	12.94	8.25	13.98	18.36	20.94	12.25	8.01	9.29	11.64	8.54
S_{ratio}	0.04	0.07	0.03	0.28	0.01	0.27	0.01	0.16	0.11	0.20	0.13	0.16
$Score$	-	-	-	-	-	-	-	-	4.39	3.59	2.77	8.81

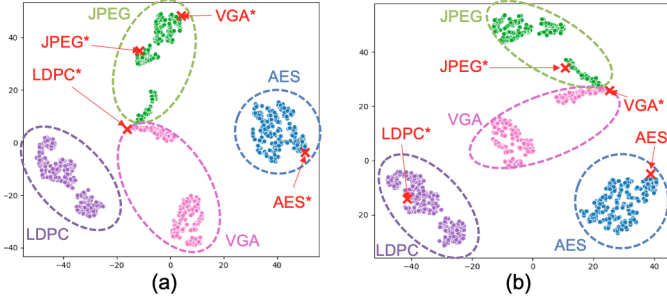


Fig. 10. Comparison between real and artificial designs by t-SNE [20]. (a) t-SNE visualization for real and artificial (ANG) designs **without** our parameter tuning flow. (b) Real and artificial (ANG) designs **with** our ML-based parameter tuning flow. Design names followed by * indicate artificial designs.

Figure 10(b) shows that with our ML-based ANG parameter tuning, datapoints of all four artificial designs are located within the corresponding clusters of real designs. This suggests that the ML-based ANG parameter tuning helps create artificial netlists that better match targeted design parameters – including parameters that are relevant to PPAC exploration.

VI. CELL WIDTH-REGULARIZED PLACEMENTS FOR MORE REALISTIC ROUTABILITY ASSESSMENT

Recall that in the PROBE approach, routability (“AC”) is evaluated using the K -threshold (K_{th}) metric [13]. That is, given a placed netlist, routing difficulty is gradually increased by iteratively swapping random pairs of neighboring instances. The cell-swaps progressively “tangle” the placement until it becomes unroutable (> 500 DRCs post-detailed routing). The number of swaps K – expressed as a multiple of the instance count – at which routing fails is the K_{th} metric. Larger K_{th} implies greater routing capacity or intrinsic routability.

Both PROBE1.0 [13] and PROBE2.0 [6] enable the study of real netlists through the concept of a *cell width-regularized* placement. In this approach, combinational cells are inflated (by LEF modification) to match the maximum width among all the combinational cells in the cell library. This process, called *cell width-regularization*, prevents illegal placements (i.e., cell overlaps due to varying widths) from arising due to neighbor-swaps during K_{th} evaluation. Unfortunately, while cell width-regularization permits real designs to be placed and then tangled by random neighbor-swaps, it also forces low utilizations that harm the realism of the study. (Moreover, high whitespace leads to high K_{th} values that require more P&R runs to determine.)

We now describe a *clustering-based cell width-regularization* methodology that generates placements with realistic utilizations, based on real designs. Our

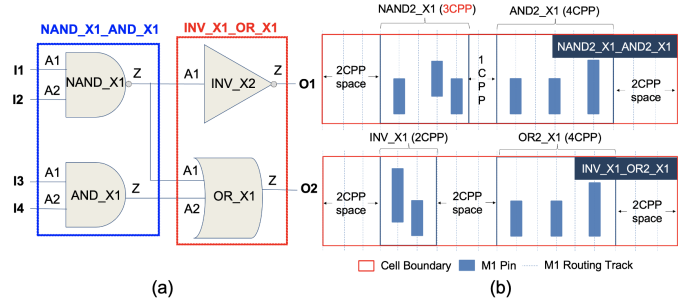


Fig. 11. Two example clustered cells NAND_X1_AND_X1, and INV_X1_OR_X1 in clustering-based cell width-regularization. (a) Schematic view, and (b) physical layout view assuming *Lib2*. Here, the maximum clustered cell width w_{max} is 12CPP.

experiments in Section VII-D show that clustering-based cell width-regularization obtains the same K_{th} rank-ordering of design enablements, with less P&R expense, than the previous cell width-regularization approach.

A. Clustering-Based Cell Width-Regularization

We propose *clustering-based cell width-regularization* using bottom-up hypergraph clustering, as detailed in Algorithm 1. In the following, we refer to standard cells of the original netlist as $cells_{orig}$, and (clustered) cells of the clustered netlist as $cells_{clustered}$.

Clustered Hypergraph Creation. For a given design, we first obtain a netlist hypergraph using OpenDB [42]. We perform *cell width-regularized clustering*, where cells $cells_{orig}$ (vertices) in the original netlist hypergraph are clustered such that *clustered cell width*⁵ does not exceed w_{max} , the maximum cell width in the library. The inputs to cell width-regularized clustering are (i) a hypergraph $H(V, E, W)$ with vertices V , hyperedges E and cell widths W , (ii) the maximum cell width, w_{max} , and (iii) a limit on number of clustering iterations, N_{iter} .⁶ The output is a clustered hypergraph (H_{out}). We use *First-Choice (FC)* clustering [14] and refer to our clustering method as *cell width-regularized clustering with FC*, or *CWR-FC*.

CWR-FC first sorts vertices in increasing order of cell widths (Line 4) and initializes *cluster assignments* (Line 6). The cluster assignment $cmap$ is the mapping of vertices to clusters (V_k to V_{k+1}). Clustered cell widths W_{k+1} are initialized in Line 7. Next, vertices are traversed in order to

⁵Given vertex set V with cell widths W , clustering vertices $v_i, v_j \in V$ yields a clustered cell with width $W[v_i] + W[v_j]$.

⁶In our experiments, we set $N_{iter} = 20$. However, the cell width-regularized clustering is strongly constrained by w_{max} , and we observe on our testcases that clustering stops after ~ 3 iterations.

Algorithm 1 Cell width-regularization by clustering.

Inputs: Hypergraph $H(V, E, W)$, Maximum cell width w_{max} . Number of iterations N_{iter}

Outputs: Clustered hypergraph $H_{out}(V_{out}, E_{out}, W_{out})$

```

1:  $N_{cluster} \leftarrow |V|$ 
2: Hypergraph at iteration 0,  $H_0(V_0, E_0, W_0) \leftarrow H(V, E, W)$ 
3: for  $k \leftarrow 0; k < N_{iter}; k++$  do
4:    $V_{ordered} \leftarrow$  Sorted  $V_k$  in increasing order of  $W_k$ 
5:    $visited[v] \leftarrow false \forall v \in V_k$ 
6:   Cluster assignments,  $cmap[v] \leftarrow v \forall v \in V_k$ 
7:   Clustered cell widths,  $W_{k+1} \leftarrow W_k$ 
8:   for  $v_i \in V_{ordered}$  do
9:     if  $visited[v_i] == true$  or  $v_i$  is a sequential cell then
10:      continue
11:      $V_{neighbor} \leftarrow$  Find adjacent vertices of  $v_i$ 
12:     Best cluster score,  $\phi_{best} \leftarrow 0$ ; Best cluster candidate,  $v_{best} \leftarrow -1$ 
13:     for  $v_j$  in  $V_{neighbor}$  do
14:       if  $W_k[v_i] + W_{k+1}[cmap[v_j]] \leq w_{max}$  then
15:          $\phi(v_i, v_j) \leftarrow \frac{\sum_{v_i \in e, v_j \in e} weight_e}{W_k[v_i] + W_{k+1}[cmap[v_j]]}$  // Cluster Score
16:         if  $\phi(v_i, v_j) > \phi_{best}$  then  $v_{best} \leftarrow v_j$ 
17:       if  $v_{best} == -1$  then
18:          $W_{k+1}[v_i] \leftarrow W_k[v_i]$ 
19:          $visited[v_i] \leftarrow true$ 
20:       else
21:          $cmap[v_i] \leftarrow cmap[v_{best}]$ 
22:          $W_{k+1}[v_{best}] \leftarrow W_k[v_i] + W_{k+1}[cmap[v_{best}]]$ 
23:          $visited[v_i] \leftarrow true; visited[v_{best}] \leftarrow true$ 
24:          $N_{cluster} \leftarrow N_{cluster} - 1$ 
25:       if  $N_{cluster} == |V_{k-1}|$  then
26:         break
27:       else
28:          $H_{k+1}(V_{k+1}, E_{k+1}, W_{k+1}) \leftarrow$  Build clustered hypergraph using  $cmap$ 
29:    $H_c \leftarrow$  Clustered hypergraph generated at last iteration
30:    $H_{out} \leftarrow$  Best-fit bin packing on  $H_c$ 
31: Return  $H_{out}$ 

```

perform pairwise clustering; note that only combinational cells are considered for clustering (Line 8). For each vertex v_i that is traversed, we find its neighbors v_j in the hypergraph (Line 11). Each v_j is considered only if it does not violate the w_{max} limit (Line 14); a cluster score $\phi(v_i, v_j)$ is calculated in Line 15. In the cluster score, $weight_e$ is the weight of hyperedge e and $W_k[v_i]$ is the width of vertex v_i . The numerator aims to cluster vertices that are strongly connected (i.e., share many hyperedges) while the denominator promotes clusters of similar widths. If all neighboring vertices v_j violate the threshold width constraint, then no new clusters are formed (Lines 17-19). Otherwise, the vertex with the highest cluster score is selected, and a new cluster is created (Lines 21-24). After all vertices are visited, we construct the clustered hypergraph and proceed with subsequent iterations (Line 28). If no further clustering is feasible, the process terminates (Line 26).

Note that *CWR-FC* clusters vertices that are adjacent to each other in the hypergraph. However, if all pairings of vertices selected for clustering violate the w_{max} width constraint, the algorithm can stall (Line 25). To address this issue and improve the uniformity of cluster contents, we perform best-fit bin-packing [11] with bins having capacity w_{max} (Line 30).⁷ Finally, the output is the clustered hypergraph H_{out} .

Clustered Netlist Creation. We convert the clustered hypergraph H_{out} into Verilog using OpenDB. Then, to run P&R we require a new LEF file that captures the cluster assignments

⁷The choice of best-fit is motivated by its simplicity and intuitiveness. Best-fit also enjoys a better approximation ratio compared to first-fit or next-fit alternatives [11].

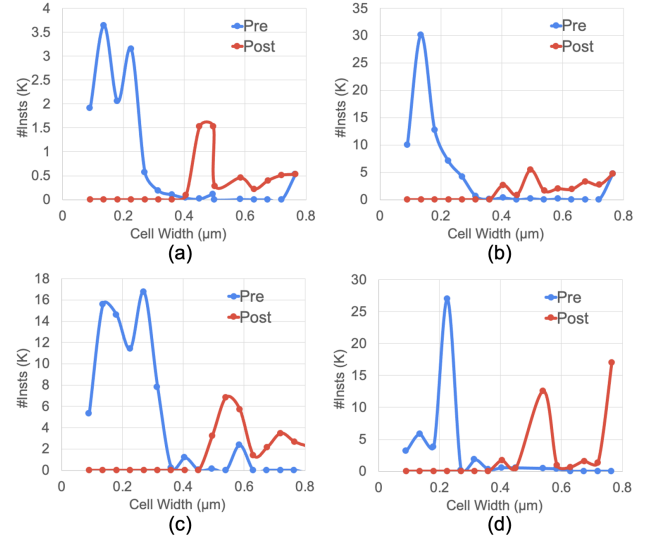


Fig. 12. Cell width distributions pre-clustering (i.e., original netlist) and post-clustering (i.e., by *CWR-FC*) for (a) AES, (b) JPEG, (c) LDPC and (d) VGA.

from cell width-regularized clustering. I.e., we require a new netlist over the clusters, $cells_{clustered}$.

Figure 11(a) provides a schematic view of two clustered cells, NAND_X1_AND_X1 and INV_X1_OR_X1. These correspond to two clusters of original cells: NAND_X1 and AND_X1, and INV_X1 and OR_X1. How the clustered cells are composed from original standard-cell layouts is shown in Figure 11(b). In this case, a non-integer gear ratio between M1P (30nm) and CPP (45nm) forces cells in $cells_{clustered}$ to be positioned at even CPP sites, to avoid M1 pin misalignment. In the first cluster, NAND_X1 width (3CPP) is an odd number of CPPs, necessitating addition of 1CPP padding between the two cells. In the second cluster, the total cell width is less than w_{max} , so whitespace is included along with the clustered original cells. We distribute whitespace uniformly, (i) at the sides of $cells_{clustered}$ and (ii) between consecutive cells in each cluster, as illustrated in Figure 11(b). During this whitespace allocation, we first allocate whitespace at junctions (between consecutive original cells) where no extra padding has been previously allocated.

B. Performance of Clustered Cell Width-Regularization

We now document advantages of our proposed clustered cell width-regularization, i.e., more realistic utilization in P&R blocks, and realistic topological and wirelength characteristics of P&R outcomes.

Comparison to Previous Cell Width-Regularization. Figure 12 compares cell width distributions for instances in the clustered netlist and instances in the original netlist. The blue lines show the distribution of cell widths in the original netlist, where smaller cell widths predominate. The red lines indicate that *CWR-FC* increases the prevalence of cells with larger widths through creation of the merged $cells_{clustered}$. The larger amount of actual cell widths in $cells_{clustered}$ leads to smaller amounts of added whitespace needed to regularize cell widths.

As anticipated, *clustered* cell width-regularization significantly reduces whitespace in the placed designs. With *Lib2* and *FSPDN* for P&R, placing cell width-regularized instances used

TABLE IX

COMPARISON OF THE WIDTH-REGULARIZED CLUSTERED NETLIST PRODUCED BY *CWR-FC* ([C]) WITH THE ORIGINAL FLAT NETLIST ([A]) AND A WIDTH-REGULARIZED CLUSTERED NETLIST INDUCED FROM A PLACEMENT OF THE FLAT NETLIST ([B]).

Stage	Design	#Insts	Area (μm^2)	Util	WL (μm)	Avg. FO
[A]	AES	12318	426.254	0.83	30849	2.32
	JPEG	70031	2781.981	0.73	112605	2.15
	LDPC	77379	6250.563	0.43	567630	1.85
	VGA	60921	4238.205	0.76	208845	2.71
[B]	AES	4275	426.254	0.83	32632	1.96
	JPEG	23281	2781.981	0.73	111241	1.86
	LDPC	42383	6250.563	0.43	585923	1.43
	VGA	40084	4238.205	0.76	189612	2.14
[C]	AES	4661	426.254	0.83	32679	2.08
	JPEG	25961	2781.981	0.73	143693	1.76
	LDPC	30636	6250.563	0.43	637417	1.29
	VGA	32768	4238.205	0.76	220915	2.02

in PROBE2.0 at 90% density achieves actual utilizations of 0.21, 0.21 and 0.40 for AES, JPEG and VGA, respectively. For LDPC, placing cell width-regularized instances at 30% density achieves actual utilization of 0.08. By contrast, with clustered cell width-regularization, we achieve actual utilizations of 0.71, 0.74 and 0.71 for AES, JPEG and VGA, respectively. For LDPC, we achieve actual utilization of 0.23. In this way, our new methodology enables K_{th} evaluation by iterated neighbor-swapping while preserving realistic placement utilizations.

Topological and Wirelength Comparisons to Real Designs.

We have confirmed additional similarities between clustered cell width-regularized netlists and the original real designs. Table IX compares characteristics of our clustering-based cell width-regularized netlists and placements ([C]), versus analogous characteristics of real netlists and placements ([A]). We also implement another plausible clustering methodology, which is to induce clusters from a placement of the original design ([B]). In [B], clusters from the placement are induced by (i) traversing combinational cells left-to-right in each standard cell row, and (ii) clustering maximal contiguous sets of cells without exceeding W_{max} .

We run P&R using *Lib2* and P_{FS} for PDN, maintaining the same core area and utilization. Clustering decreases the number of instances and average fanouts for [B] and [C], relative to [A]. However, wirelengths exhibit no significant changes. The similarities between [A], [B] and [C] suggest that our *CWR-FC* methodology can preserve netlist properties relevant to P&R outcomes, with more realistic placement utilizations.

VII. EXPERIMENTAL SETUP AND RESULTS

We have extensively studied the design-technology pathfinding capability of the PROBE3.0 framework using the PROBE3.0 technology. In this section, we report three main experiments. Expts 1 and 2 show PROBE3.0's capability to assess PPAC trends and tradeoffs, using real and artificial designs respectively. Expt 3 performs assessments of routability and achievable utilization.

In Expts 1 and 2, we analyze four tradeoffs. (i) We present *Performance-Power* plots that quantify tradeoffs between performance (maximum frequency) and power. (ii) We present *Performance-Area* plots to quantify the tradeoffs between performance and area. (iii) To address PP aspects, we use the *Energy-Delay Product* (EDP) [18] as a single metric

for power and performance. *EDP-Area* plots depict tradeoffs between performance/power and area. (iv) We present *IR drop-Area* plots to demonstrate tradeoffs between IR drop and area. We also compare results obtained using artificial designs with those obtained using real designs. Expt 3 assesses routability and achievable utilization using our clustering-based cell width-regularized placements.

A. Experimental Setup

Based on the definition of technology and design parameters in [6], we define ten technology parameters and eight design parameters as the input parameters for the PROBE3.0 framework. Table X describes the definitions of these parameters and the options used in our experiments. Also, we use commercial tools for PDK generation, logic synthesis, P&R, and IR drop analysis. We use open-source tools for GDT-to-GDS translation [38] and SMT solver [49]. Table XI summarizes the tools and versions that we use in our experiments.

Criteria for Valid Result. In our experiments, for given *Design*, *PDN* and technology parameters, we perform logic synthesis, P&R and IR drop analysis with multiple sets of parameters including I_{pitch} , I_{scheme} , $Util$ and $Clkp$. We use 24, 32, 48, 96 and 128 *CPP* for I_{pitch} , and *Column* and *Staggered* for I_{scheme} . For $Util$, we use values ranging from 0.70 to 0.94 with a step size of 0.02, and for $Clkp$, we use values ranging from 0.12 to 0.24ns with a step size of 0.02ns. Importantly, after the implementation and the analysis steps, we filter out results that are deemed invalid – in that they are likely to fail signoff criteria even with additional human engineering efforts.

To be precise, a “valid” result must satisfy three conditions: (i) the worst negative slack is larger than -50ps; (ii) the number of post-route DRCs is less than 500; and (iii) the 99.7 percentile of the effective instance voltage is greater than 80% of the operating voltage (V_{op}). To assess (iii), we use a commercial IR drop analysis tool [36] to measure vectorless dynamic IR drop, and calculate the effective instance voltage as $V_{op} - V_{drop}$ per each instance, where V_{op} is an operating voltage (0.7V) and V_{drop} is the worst voltage drop per instance. We take the 99.7 percentile of effective instance voltage as representative of IR drop for the post-P&R result, as it is within three standard deviations from the mean per the empirical rule [28].

B. Expt 1 (PPAC Exploration with Real Designs)

Performance versus Power. We first present PPAC explorations that show tradeoffs between performance and power. (We assume that area is proportional to cost, since chip area is closely related to cost.) In this study, we show results for JPEG with four standard-cell libraries (*Lib1-4*). Also, we use four PDN structures, P_{FS} , P_{FB} , P_{BS} and P_{BB} , and measure improvements due to scaling boosters relative to the traditional frontside PDN (P_{FS}).

Figure 13(a) gives *Performance-Power* plots that show tradeoffs between performance and power for JPEG, and improvements from the traditional FSPDN. We calculate the maximum achievable frequency (f_{max}) as $1/(Clkp - WNS)$ where $Clkp$ is the target clock period and WNS is the worst negative slack. Also, we add up leakage and dynamic power

TABLE X
TECHNOLOGY AND DESIGN PARAMETERS IN OUR EXPERIMENTS.

Type	Parameter	Description	Option
Technology	F_{in}	The number of fins for devices of standard cells.	2, 3
	CPP	Contacted poly pitch for standard cells in nm .	45
	$M0P$	M0 (horizontal) layer pitch in nm .	24
	$M1P$	M1 (vertical) layer pitch in nm .	30
	$M2P$	M2 (horizontal) layer pitch in nm .	24
	RT	The number of available M0 routing tracks in standard cells.	4, 5
	$PGpin$	Power/ground pin layer for standard cells.	$BPR, M0$
	CH	Cell height of standard cells, expressed as a multiple of $M0P$. For example, when the cell height in nm is $120nm$ and $M0P$ is $24nm$, the cell height (CH) is 5. The cell height value is calculated as $RT + 2$ for $M0 PGpin$ and $RT + 1$ for $BPR PGpin$.	5, 6, 7
	MPO	The number of minimum pin openings (access points).	2
Design	DR	Design rules. We define the same grid-based design rules, minimum area rule ($DR-MAR$), end-of-line spacing rule ($DR-EOL$) and via spacing rule ($DR-VR$) as [6]. We use the <i>EUV-tight</i> (ET) design rule set, which includes $DR-MAR = 1$, $DR-EOL = 2$ and $DR-VR = 1$.	<i>EUV-Tight</i>
	$BEOL$	Metal stack options. We define 14M metal option which contains 14 metal layers (M0 to M13). We define 1.2X, 2.6X, 3.2X and 30X layer pitches based on 24nm as the 1X pitch.	14M
	PDN	Power delivery network options.	$P_{FS}, P_{FB}, P_{BS}, P_{BB}$
	I_{pitch}	Power tap cell pitch in CPP.	24, 32, 48, 96, 128
	I_{scheme}	Power tap cell insertion scheme.	<i>Column, Staggered</i>
	$Tool$	Commercial P&R tools.	<i>Synopsys IC Compiler II</i>
	$Util$	Initial placement utilization.	0.70 to 0.94 with a 0.02 step size
	$Design$	Designs studied in our experiments. We conduct experiments with four open-source designs from OpenCores [41] and artificial netlists generated by ANG with our ML-based parameter tuning.	AES, JPEG
	$Clkp$	Target clock period for logic synthesis and P&R. We define target clock periods that reflect maximum achievable frequencies of the designs.	0.12 to 0.24ns with a 0.02ns step size

TABLE XI
TOOLS AND VERSIONS IN OUR EXPERIMENTS.

Purpose	Tool	Version	Ref.
Format Conversion	<i>GDT-to-GDS translator</i>	4.0.4	[38]
IR Drop Analysis	<i>Cadence Voltus</i>	19.1	[36]
Library Characterization	<i>Cadence Liberate</i>	16.1	[33]
Logic Synthesis	<i>Cadence Genus</i>	21.1	[32]
	<i>Synopsys Design Compiler</i>	R-2020.09	[44]
LVS	<i>Siemens Calibre</i>	2017.4_19	[43]
P&R	<i>Synopsys IC Compiler-II</i>	R-2020.09	[45]
PEX	<i>Cadence QRC Extraction</i>	19.1	[35]
	<i>Synopsys StarRC</i>	O-2018.06	[46]
	<i>Siemens Calibre</i>	2017.4_19	[43]
SMT solver	<i>Z3</i>	4.8.5	[9][49]

to obtain the total power. To measure the improvement from P_{FS} , we compare the second-largest value (on the x-axis) attained with each PDN configuration. From the result, we make two main observations. (i) Power consumption with P_{BS} and P_{BB} decreases by 7 to 8%, compared to P_{FS} with the same performance. (ii) Power consumption with P_{FB} is similar to P_{FS} , with the same performance. We observe power reductions from use of scaling boosters, BSPDN and BPR. However, use of BPR without BSPDN does not reduce power consumption.

Performance versus Area. Performance-area tradeoffs for JPEG are shown in Figure 13(b). We make two main observations. (i) Area with P_{FB} , P_{BS} and P_{BB} decreases by up to 8%, 5% and 24%, respectively, as compared to P_{FS} , while maintaining the same level of performance. (ii) We find that use of scaling boosters results in area reductions across all four standard-cell libraries. The area reduction results obtained using the PROBE3.0 framework are consistent with previous industry works [10][22][29][31], which show that use of BSPDN and BPR techniques can result in area reductions of 25% to 30%.

Energy-Delay Product (EDP) versus Area. Given the tradeoffs among PPAC criteria, a simpler metric is useful to comprehend multiple aspects simultaneously. The *Energy-Delay Product* (EDP) is adopted by, e.g., [18] as a single-value metric that captures both power efficiency and maximum achievable frequency (performance). EDP is calculated as

$P \times f_{max}^2$, where P denotes power consumption and f_{max} denotes maximum achievable frequency. Lower EDP means more energy-efficient operations for the chip. Since we address power, performance and area (cost), we draw *EDP-Area* plots to show PPAC tradeoffs of various PDN structures. We again use four standard-cell libraries (*Lib1-4*).

From Figure 13(c), we derive four key observations. (i) For $4RT$ (*Lib1* and *Lib2*), EDP with P_{FB} , P_{BS} and P_{BB} decreases by 0.2, 0.2 and 0.4 $mW \cdot ns^2$, respectively, compared to P_{FS} with the same area. (ii) For $5RT$ (*Lib3* and *Lib4*), EDP with P_{BB} decreases by 0.3 $mW \cdot ns^2$, compared to P_{FS} with the same area. (iii) For $5RT$, EDP with P_{FB} shows no improvements, and EDP with P_{BS} increases by 0.1 $mW \cdot ns^2$, as compared to P_{FS} with the same area. (iv) Use of P_{BB} better optimizes area than other PDN structures with the same EDP. **Supply Voltage (IR) Drop versus Area.** With recent advanced technologies and designs, denser PDN structures are required due to large resistance seen in tight-pitch BEOL metal layers. The denser PDN structures bring added routability challenges which critically impact area density. In light of this, we measure IR drop and area from valid runs, and plot *IR drop-Area* tradeoffs in Figure 14. In the plots, we compare the points with the minimum area for each PDN configuration in terms of area and 99.7 percentile (three-sigma) of effective instance voltage (EIV). Note that larger effective instance voltage means better IR drop mitigation. Figures 14(a) and (b) show *IR drop-Area* tradeoffs for JPEG with $4RT$ (*Lib1* and *Lib2*) and $5RT$ (*Lib3* and *Lib4*), respectively. From the results, we make four main observations. (i) Area with P_{FB} decreases by 2 to 6% compared to P_{FS} , while the effective instance voltage (EIV) increases by 3 to 4%. (ii) Area with P_{BS} increases by 1 to 4% compared to P_{FS} , while EIV decreases by 4 to 12%. (iii) Area with P_{BB} decreases by 15 to 18% compared to P_{FS} , while EIV decreases by 17%. (iv) We observe that there is IR drop mitigation from use of backside PDN, while use of BPR (P_{FB}) worsens IR drop. This implies that more power tap cells will need to be inserted to mitigate IR drop. However, the area overhead of power tap cells will

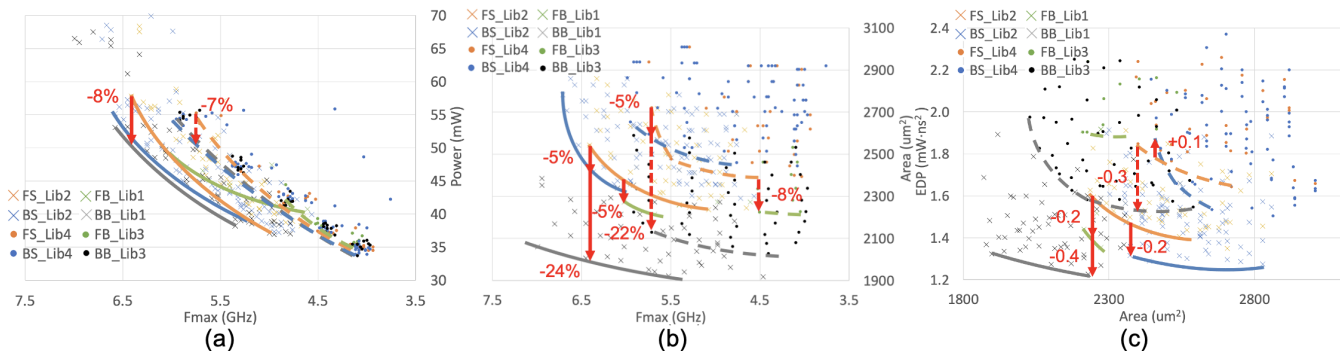


Fig. 13. PPAC tradeoffs for JPEG with four standard-cell libraries (*Lib1*, *Lib2*, *Lib3* and *Lib4*). We compare four PDN structures in terms of performance and area and measure improvements relative to traditional frontside PDN (P_{FS}), in order to show the benefits of the scaling boosters (BSPDN and BPR). We draw plots for (a) *Performance-Power*, (b) *Performance-Area*, and (c) *Energy-Delay Product-Area*.

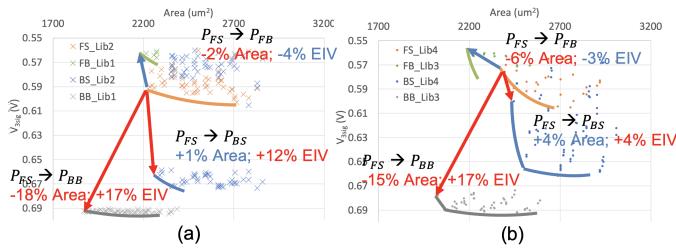


Fig. 14. *IR drop-Area* plots for JPEG with four standard-cell libraries (*Lib1*, *Lib2*, *Lib3* and *Lib4*). (a) JPEG with 4RT (*Lib1/2*), and (b) JPEG with 5RT (*Lib3/4*).

degrade the IR drop quality achieved by use of BPR.

C. Expt 2 (PPAC Exploration with Artificial Design)

Our second main experiment uses the *artificial JPEG* design generated by ANG using our ML-based parameter tuning. We conduct the same studies as in Expt 1 and analyze the results.

Performance versus Power. Figure 15(a) shows the tradeoffs between performance and power with the artificial JPEG design. From the result, we make three main observations. (i) Power consumption with P_{BS} and P_{BB} decreases by 6 to 14%, compared to P_{FS} with the same performance. (ii) Power consumption with P_{FB} is similar to P_{FS} with the same performance. (iii) Results with the artificial JPEG show up to 7% differences, but with similar trends, compared to the results obtained with the real JPEG design.

Performance versus Area. Figure 15(b) shows tradeoffs between performance and area with the artificial JPEG design. We make three main observations. (i) Area with P_{FB} and P_{BB} decreases up to 14% and 21% compared to P_{FS} with the same performance. (ii) Area with P_{BS} increases by 0% to 3% compared to P_{FS} with the same performance. This area penalty is caused by power tap cell insertion for P_{BS} . (iii) We observe that the results with the artificial JPEG show up to 9% differences, but with similar trends, compared to the results obtained with the real JPEG design. However, area for P_{BS} shows opposite trends to what we observe with the real design, although the discrepancy is not too large.

Energy-Delay Product (EDP) versus Area. From Figure 15(c), we make three main observations. (i) For 4RT (*Lib1* and *Lib2*), EDP with P_{BB} decreases by $0.5 \text{ mW} \cdot \text{ns}^2$, compared to P_{FS} with the same area. However, EDP with P_{FB} and P_{BS} shows no improvements. (ii) For 5RT (*Lib3*

and *Lib4*), EDP with P_{FB} and P_{BB} decreases by 0.6 and 0.9 $\text{mW} \cdot \text{ns}^2$, compared to P_{FS} with the same area. However, EDP with P_{BS} shows no improvements. (iii) We observe that results with the artificial JPEG show similar trends as results obtained with the real JPEG design.

Supply Voltage (IR) Drop versus Area. Figures 16(a) and (b) show tradeoffs between IR drop and area for the artificial JPEG design with 4RT (*Lib1* and *Lib2*) and 5RT (*Lib3* and *Lib4*), respectively. We make four main observations. (i) Area with P_{FB} decreases by 9 to 14%, compared to P_{FS} , while the effective instance voltage (EIV) increases by 1 to 6%. (ii) Area with P_{BS} increases by 2%, compared to P_{FS} , while EIV decreases by 2 to 3%. (iii) Area with P_{BB} decreases by 14 to 18%, compared to P_{FS} , while EIV decreases by 6 to 11%. (iv) We observe that results with the artificial JPEG show similar trends as results obtained with the real JPEG design, and that discrepancies are reasonably small.

D. Expt 3 (Routability Assessment and Achievable Utilization)

Our third main experiment measures K_{th} using our *clustering-based cell width-regularized placements* (Section VI), and explores the relationship between K_{th} and achievable utilization. We note that the previous work of [6] introduced *Achievable Utilization* as the maximum utilization for which the number of DRCs is less than a predefined threshold of 500 DRCs. Here, we include all three criteria for a valid result (Section VII-A), and define *Achievable Utilization* as the maximum utilization among all valid runs seen.

Figure 17 shows experimental results for K_{th} and achievable utilization. We conduct our experiment with artificial JPEG and four cell width-regularized libraries (*Lib1-4*). From the plots, we make two observations. (i) We compare the results with 2Fin/4RT standard-cell libraries (*Lib1/2*) to those with 3Fin/5RT standard-cell libraries (*Lib3/4*). The data show that a larger number of M0 routing tracks brings better routability. (ii) Compared to P_{FS} , P_{FB} and P_{BB} , the plots for P_{BS} are skewed to the right for each design, showing better routability than the other PDN configurations. We observe that the routability improvement of P_{BS} comes from regularly-placed power tap cells: the power tap cell placement eases routing congestion caused by high cell and/or pin density.

Finally, we compare the K_{th} results obtained with the previous *cell width-regularized placements* used in the PROBE2.0 work ([A]) and *clustering-based cell width-regularized place-*

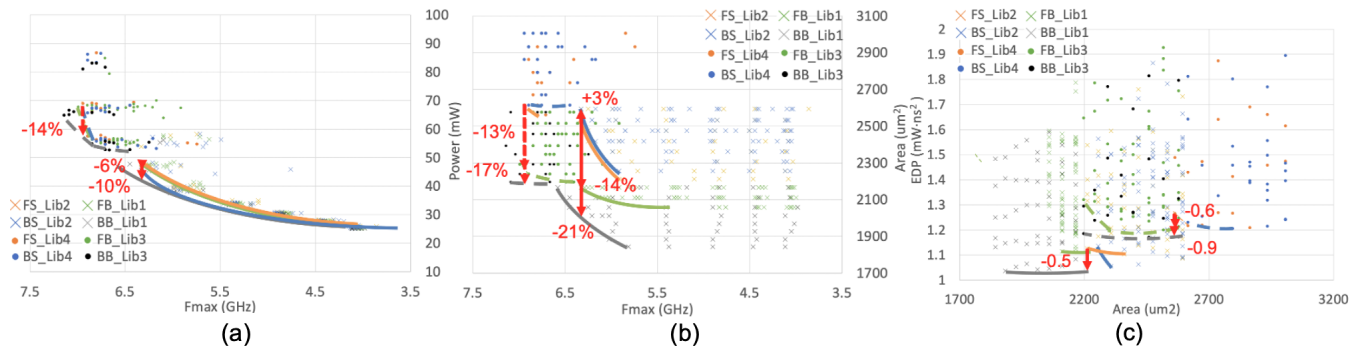


Fig. 15. PPAC tradeoffs for “artificial” JPEG with four standard-cell libraries (*Lib1*, *Lib2*, *Lib3* and *Lib4*). Shown: (a) Performance-Power, (b) Performance-Area, and (c) Energy-Delay Product-Area.

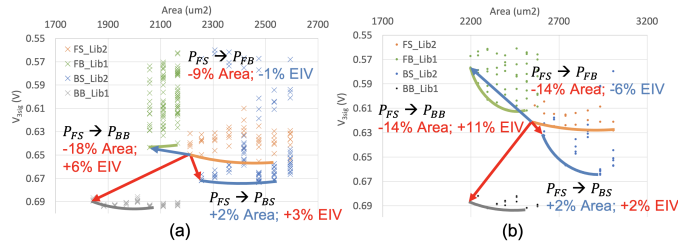


Fig. 16. IR drop-Area plots for “artificial” JPEG with four standard-cell libraries (*Lib1*, *Lib2*, *Lib3* and *Lib4*). (a) JPEG with 4RT (*Lib1/2*), and (b) JPEG with 5RT (*Lib3/4*).

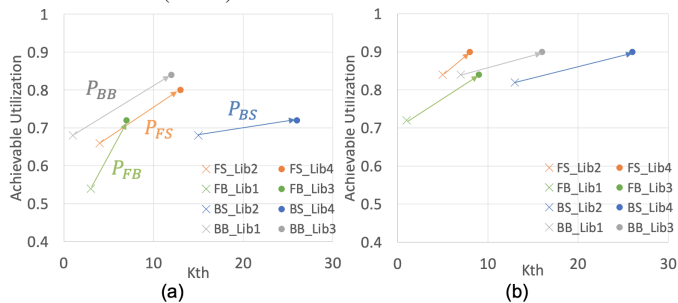


Fig. 17. K_{th} and achievable utilization for (a) AES and (b) JPEG, with various libraries and power delivery methodologies.

ments obtained using the *CWR-FC* algorithm of Section VI-A ([C]). We perform routability assessments as summarized in Table XII. We rank-order K_{th} across the eight combinations of four *PDN* and two *RT* with the JPEG design. The main observation from this comparison is that the ordering of enablements based on K_{th} is the same for both placements, even as the area utilization of the *clustering-based cell width-regularized placements* is closer to the initial utilization (0.6). We conclude that our *clustering-based cell width-regularized placement* methodology successfully provides more realistic placements without disrupting the K_{th} -based rank-ordering of enablements. Moreover, the generally smaller K_{th} values seen in the rightmost two columns of Table XII imply fewer P&R trials needed to evaluate the K_{th} metric.

VIII. CONCLUSION

We have presented PROBE3.0, a systematic and configurable framework for “full-stack” PPAC exploration and pathfinding in advanced technology nodes. We introduce automated PDK and standard-cell library generation, along with enablement of scaling boosters in a predictive 3nm technology. Our work is permissively open-sourced in GitHub [48], and

TABLE XII

K_{th} COMPARISON FOR THE JPEG DESIGN WITH *cell width-regularized placements* ([A]) AND *clustering-based cell width-regularized placements* ([C]). *Util* DENOTES REAL UTILIZATION WITH 0.6 INITIAL UTILIZATION.

Rank	<i>PDN</i>	<i>RT</i>	Library	[A]		[C]	
				K_{th}	<i>Util</i>	K_{th}	<i>Util</i>
1	P_{FB}	4	<i>Lib1</i>	6	0.14	3	0.50
2	P_{FS}	4	<i>Lib2</i>	9	0.14	5	0.49
3	P_{BB}	4	<i>Lib1</i>	12	0.14	7	0.50
4	P_{FS}	5	<i>Lib4</i>	15	0.14	8	0.50
5	P_{FB}	5	<i>Lib3</i>	16	0.14	9	0.50
6	P_{BS}	4	<i>Lib2</i>	17	0.14	13	0.49
7	P_{BB}	5	<i>Lib3</i>	18	0.14	16	0.50
8	P_{BS}	5	<i>Lib4</i>	23	0.14	26	0.50

includes open-sourceable PDKs and EDA tool scripts that incorporate power and performance considerations into the framework.

We employ artificial netlist generation with a machine learning-based parameter tuning to mimic properties of arbitrary real designs. Along with a new *CWR-FC* clustering-based width-regularized netlist and placement methodology, this enables PPAC exploration of a much wider space of technology, design enablement, and design options. From our experiments, we find that the use of backside power delivery network (BSPDN) and buried power rails (BPR) can lead to up to 8% reduction in power consumption and up to 24% reduction in area using our predictive 3nm technology. These results from PROBE3.0 closely match previous works [10][22][29][31] which estimated 25% to 30% area reduction from use of BSPDN and BPR.

Ongoing and future directions include the following. (i) Improving the software architecture of PROBE3.0 will make it more accessible and flexible for users to pursue their own PPAC explorations. Supporting the addition of user-defined variables can help capture and study variant technology and design assumptions. (ii) To improve robustness of the framework, and its usefulness as a “proxy” in real-world advanced technology development and DTCO, improved device models, parasitic extraction models, signoff corner definitions, relevant design examples, etc. will be beneficial. It will also be necessary to add generation of DRC rule decks for commercial tools. (iii) While our scripts for commercial tools are shared publicly in our GitHub repository, using these tools still requires valid licenses. Incorporation of open-source tools into the PROBE3.0 framework can potentially lead to highly-scaled deployments, shorter turnaround times, and improved utility to

a broader audience.

ACKNOWLEDGMENTS

We thank Dr. Mustafa Badaroglu at Qualcomm, Dr. Gi-Joon Nam at IBM, Dr. S. C. Song at Google and Prof. Taigon Song at Kyungpook National University for valuable discussions.

REFERENCES

- [1] A. Agnesina, K. Chang and S. K. Lim, "VLSI Placement Parameter Optimization using Deep Reinforcement Learning", *Proc. ACM/IEEE Intl. Conf. on Computer-Aided Design*, 2020, pp. 1-9.
- [2] K. Bhanushali and W. R. Davis, "FreePDK15: An Open-Source Predictive Process Design Kit for 15nm FinFET Technology", *Proc. ACM Intl. Symp. on Physical Design*, 2015, pp. 165–170.
- [3] D. Chanemougame, J. Smith, P. Gutwin, B. Byrns and L. Liebmann, "Agile Pathfinding Technology Prototyping: the Hunt for Directional Correctness", *Proc. International Conference on Simulation of Semiconductor Processes and Devices*, 2020, pp. 301-305.
- [4] B. Chava, K. A. Shaik, A. Jourdain, S. Guissi, P. Weckx, J. Ryckaert, G. Van Der Plaas, A. Spessot, E. Beyne and A. Mocuta, "Backside Power Delivery as a Scaling Knob for Future Systems", *Proc. SPIE 10962, Design-Process-Technology Co-optimization for Manufacturability XIII 1096205* (2019), pp. 1-6.
- [5] C.-K. Cheng, C.-T. Ho, C. Holtz and B. Lin, "Design and System Technology Co-Optimization Sensitivity Prediction for VLSI Technology Development using Machine Learning", *Proc. ACM/IEEE Intl. Workshop on System-Level Interconnect Prediction*, 2021, pp. 1-8.
- [6] C.-K. Cheng, A. B. Kahng, H. Kim, M. Kim, D. Lee, D. Park and M. Woo, "PROBE2.0: A Systematic Framework for Routability Assessment from Technology to Design in Advanced Nodes", *IEEE Trans. on CAD 41(5)* (2022), pp. 1495-1508.
- [7] C. Chidambaram, A. B. Kahng, M. Kim, G. Nallapati, S. C. Song and M. Woo, "A Novel Framework for DTCO: Fast and Automatic Routability Assessment with Machine Learning for Sub-3nm Technology Options", *Proc. IEEE Symposium on VLSI Technology*, 2021, pp. 1-2.
- [8] L. T. Clark, V. Vashishtha, L. Shifren, A. Gujja, S. Sinha, B. Cline, C. Ramamurthy and G. Yeric, "ASAP7: A 7-nm FinFET Predictive Process Design Kit", *Microelectronics Journal* 53 (2016), pp. 105–115.
- [9] L. De Moura and N. Bjørner, "Z3: An Efficient SMT Solver", *Proc. Intl. Conf. on Tools and Algorithms for the Construction and Analysis of Systems*, 2008, pp. 337–340.
- [10] M. O. Hossen, B. Chava, G. Van der Plas, E. Beyne and M. S. Bakir, "Power Delivery Network (PDN) Modeling for Backside-PDN Configurations With Buried Power Rails and μ TSVs", *IEEE Trans. on Electron Devices* 67(1) (2020), pp. 11-17.
- [11] D. Johnson, "Near-optimal Bin Packing Algorithms", *Ph.D. Thesis*, Massachusetts Institute of Technology, 1973.
- [12] A. B. Kahng, S. Kang, S. Kim and B. Xu, "Enhanced Power Delivery Pathfinding for Emerging 3D Integration Technology", *IEEE Trans. on VLSI* 29(4) (2021), pp. 591-604.
- [13] A. Kahng, A. B. Kahng, H. Lee and J. Li, "PROBE: Placement, Routing, Back-End-of-Line Measurement Utility", *IEEE Trans. on CAD 37(7)* (2018), pp. 1459-1472.
- [14] G. Karypis, R. Aggarwal, V. Kumar and S. Shekhar, "Multilevel Hypergraph Partitioning: Applications in VLSI Domain", *IEEE Trans. on VLSI* 7(1) (1999), pp. 69-79.
- [15] T. Kim, J. Jeong, S. Woo, J. Yang, H. Kim, A. Nam, C. Lee, J. Seo, M. Kim, S. Ryu, Y. Oh and T. Song, "NS3K: A 3-nm Nanosheet FET Standard Cell Library Development and Its Impact", *IEEE Trans. on VLSI* 31(2) (2023), pp. 163-176.
- [16] D. Kim, S.-Y. Lee, K. Min and S. Kang, "Construction of Realistic Place-and-Route Benchmarks for Machine Learning Applications", *IEEE Trans. on CAD* (2022), doi:10.1109/TCAD.2022.3209530.
- [17] E. D. Kurmiawan, H. Yang, C.-C. Lin and Y.-C. Wu, "Effect of Fin Shape of Tapered FinFETs on the Device Performance in 5-nm Node CMOS Technology", *Microelectronics Reliability* 83 (2018), pp. 254-259.
- [18] L. Liebmann, D. Chanemougame, P. Churchill, J. Cobb, C.-T. Ho, V. Moroz and J. Smith, "DTCO Acceleration to Fight Scaling Stagnation", *Proc. SPIE 11328, Design-Process-Technology Co-optimization for Manufacturability XIV*, 2020, 113280C, pp. 1-15.
- [19] L.-C. Lu, "Physical Design Challenges and Innovations to Meet Power, Speed, and Area Scaling Trend", *Proc. ACM Intl. Symp. on Physical Design*, 2017, pp. 63.
- [20] L. Maaten and G. Hinton, "Visualizing Data Using t-SNE", *Journal of Machine Learning Research* 9 (2008), pp. 2579-2605.
- [21] D. Prasad, S. S. T. Nibhanupudi, S. Das, O. Zografos, B. Chehab, S. Sarkar, R. Baert, A. Robinson, A. Gupta, A. Spessot, P. Debacker, D. Verkest, J. Kulkarni, B. Cline and S. Sinha, "Buried Power Rails and Back-side Power Grids: Arm® CPU Power Delivery Network Design Beyond 5nm", *Proc. IEEE International Electron Devices Meeting*, 2019, pp. 19.1.1-19.1.4.
- [22] J. Ryckaert *et al.*, "Extending the Roadmap Beyond 3nm through System Scaling Boosters: A Case Study on Buried Power Rail and Backside Power Delivery", *Proc. Electron Devices Technology and Manufacturing Conference*, 2019, pp. 50-52.
- [23] S. Sadangi, "FreePDK3: A Novel PDK for Physical Verification at the 3nm Node", *M.S. Thesis*, Computer Engineering, North Carolina State University, 2021.
- [24] G. Sisto *et al.*, "IR-Drop Analysis of Hybrid Bonded 3D-ICs with Backside Power Delivery and μ - & n-TSVs", *Proc. IEEE International Interconnect Technology Conference*, 2021, pp. 1-3.
- [25] S. C. Song *et al.*, "Unified Technology Optimization Platform using Integrated Analysis (UTOPIA) for Holistic Technology, Design and System Co-Optimization at \leq 7nm Nodes", *Proc. IEEE Symposium on VLSI Circuits*, 2016, pp. 1-2.
- [26] H. Su, J. Hu, S. S. Sapatnekar and S. R. Nassif, "Congestion-Driven Codesign of Power and Signal Networks", *Proc. ACM/ESDA/IEEE Design Automation Conference*, 2002, pp. 64-69.
- [27] S. S. Teja Nibhanupudi, D. Prasad, S. Das, O. Zografos, A. Robinson, A. Gupta, A. Spessot, P. Debacker, D. Verkest, J. Ryckaert, G. Helling, J. Myers, B. Cline and J. P. Kulkarni, "A Holistic Evaluation of Buried Power Rails and Back-Side Power for Sub-5nm Technology Nodes", *IEEE Trans. on Electron Devices* 69(8) (2022), pp. 4453-4459.
- [28] 68-95-99.7 Rule. https://en.wikipedia.org/wiki/68-95-99.7_rule
- [29] Applied Materials Logic Master Class. <https://ir.appliedmaterials.com/static-files/acba6be3-4778-41eb-9183-5c8e52884dea>
- [30] Artificial Netlist Generator. https://github.com/daeyeon22/artificial_netlist_generator
- [31] D. O'Laughlin, "Backside Power Delivery and Bold Bets at Intel", June 2022. <https://www.fabricatedknowledge.com/p/backside-power-delivery-and-bold>
- [32] Cadence Genus User Guide. <http://www.cadence.com>
- [33] Cadence Liberate User Guide. <http://www.cadence.com>
- [34] Cadence PVS User Guide. <http://www.cadence.com>
- [35] Cadence QRC Extraction User Guide. <http://www.cadence.com>
- [36] Cadence Voltus User Guide. <http://www.cadence.com>
- [37] FreePDK3 Predictive Process Design Kit. <https://github.com/ncsu-eda/FreePDK3>
- [38] GDT to GDS Format Translator. <https://sourceforge.net/projects/gds2>
- [39] H2O AutoML. <https://www.h2o.ai>
- [40] IEEE International Roadmap for Devices and Systems (IRDS), 2020 Edition. <https://irds.ieee.org/editions/2020>
- [41] OpenCores: Open Source IP-Cores. <http://www.opencores.org>
- [42] OpenDB. <https://github.com/The-OpenROAD-Project/OpenDB>
- [43] Siemens EDA Calibre User Guide. <https://eda.sw.siemens.com/en-US/ic/calibre-design/>
- [44] Synopsys Design Compiler User Guide. <http://www.synopsys.com>
- [45] Synopsys IC Compiler II User Guide. <http://www.synopsys.com>
- [46] Synopsys StarRC User Guide. <http://www.synopsys.com>
- [47] Synopsys DTCO Flow: Technology Development. <https://www.synopsys.com/silicon/resources/articles/dtco-flow.html>
- [48] The PROBE3.0 Framework. <https://github.com/ABKGroup/PROBE3.0>
- [49] Z3 SMT Solver. <https://github.com/Z3Prover/z3>